Available online at www.sciencedirect.com
SCIENCE DIRECT®
Applied Numerical Mathematics 56 (2006) 1211–1224
APPLIED NUMERICAL MATHEMATICS
www.elsevier.com/locate/apnum

Mapped WENO and weighted power ENO reconstructions in semi-discrete central schemes for Hamilton–Jacobi equations

Steve Bryson [a,*], Doron Levy [b,1]

[a] *NASA Advanced Supercomputing Division, NASA Ames Research Center, Moffett Field, CA 94035-1000, USA*
[b] *Department of Mathematics, Stanford University, Stanford, CA 94305-2125, USA*

Available online 15 May 2006

Abstract

We incorporate new high-order WENO-type reconstructions into Godunov-type central schemes for Hamilton–Jacobi equations. We study schemes that are obtained by combining the Kurganov–Noelle–Petrova flux with the weighted power ENO and the mapped WENO reconstructions. We also derive new variants of these reconstructions by composing the weighted power ENO and the mapped WENO reconstructions with each other. While all schemes are, formally, fifth-order accurate, we show that the quality of the approximation does depend on the particular reconstruction that is being used. In certain cases, it is shown that the approximate solution may not converge to the viscosity solution at all.

MSC: primary 65M06; secondary 35L99

Keywords: Hamilton–Jacobi equations; Central schemes; Semi-discrete schemes; High order; WENO; Weighted power ENO; Mapped ENO

1. Introduction

In this work we are interested in numerical approximations to solutions of multidimensional Hamilton–Jacobi equations of the form

$$\phi_t + H(\nabla\phi) = 0, \quad \vec{x} = (x_1, \ldots, x_d) \in \mathbb{R}^d, \tag{1}$$

where $\phi = \phi(\vec{x}, t)$, and the Hamiltonian, H, depends on $\nabla\phi$ and possibly on $\vec{x}$ and t. Solutions of (1) typically develop discontinuous derivatives in finite time even when the initial data is smooth and hence they should be studied in a suitable weak formulation. Such a weak formulation is given by the so-called *viscosity solutions* (see [7,8,19,20,28] and the references therein).

In recent years, there have been many advances in the derivation and the analysis of numerical approximations for the time-dependent problem (1). Among the approaches that are relevant to the present work we mention the upwind ENO methods of Osher, Sethian, and Shu [24,25], that are based on the "essentially non-oscillatory" (ENO) reconstruction of Harten et al. [10]. A more compact high-order scheme is due to Jiang and Peng [12] and is based on

* Corresponding author.
E-mail addresses: sbryson@mail.arc.nasa.gov (S. Bryson), dlevy@math.stanford.edu (D. Levy).
[1] The work of D. Levy was supported in part by the National Science Foundation under Career Grant No. DMS-0133511.

0168-9274/$30.00
doi:10.1016/j.apnum.2006.03.005

the weighted ENO (WENO) reconstruction (first used for approximating solutions of hyperbolic conservation laws [13,23]). Extensions to triangular meshes can be found in [1,29].

A related approach is of Godunov-type central schemes, introduced by Lin and Tadmor [21,22]. There, the idea is to avoid dealing with discontinuities (and the resulting Riemann problems) by averaging over the singularities. In [3–5] we extended the Lin–Tadmor schemes to third and fifth order. These high-order extensions were obtained by incorporating suitable WENO reconstructions into the central framework. A semi-discrete formulation of central schemes is due to Kurganov et al. [14,16]. This semi-discrete limit was obtained by keeping track over the local speeds of propagation of information from the discontinuities. Once again, with the aid of WENO reconstructions, we extended the order of accuracy of these schemes to fifth-order [6]. We also introduced a variant with reduced numerical dissipation in [2]. Recently, we also announced the extension of these schemes to triangular meshes [17,18].

Instead of distinguishing between upwind and central schemes, an alternative way of thinking about them, at least in the semi-discrete case, is by considering these schemes as being composed of the following three building blocks: a (monotone) numerical flux, a high-order reconstruction, and an ODE solver. In our previous works we have emphasized the role of the numerical flux. For example, in [6] we showed that replacing the widely used local Lax–Friedrichs flux with the central flux of [14], may reduce the errors by as much as an order of magnitude (when compared with [12]).

The goal of this work is to study the role of the reconstruction on the quality of the numerical approximations with central schemes. With this in mind, we explore two relatively new ideas in the theory of high-order WENO approximations: the weighted power ENO reconstruction of Serna et al. [26,27], and the mapped WENO of Henrick et al. [11]. The basic idea of the power ENO scheme is to apply an extended class of limiters to classical ENO schemes in order to improve the algorithmic behavior near discontinuities. The mapped WENO interpolants, on the other hand, improve the accuracy of the WENO reconstructions, by using a nonlinear mapping of the WENO weights. Our approach is to combine the numerical flux of [14] with the reconstructions from [11,27]. While the weighted power ENO schemes were used (in conjunction with upwind fluxes) for HJ equations [27], the mapped WENO reconstructions are used for HJ equations in this work for the first time. In addition, we conduct a study on the effect of composing the mapped WENO reconstruction on top of the weighted power ENO interpolant. These two interpolants are combined in this work for the first time.

Our results indicate that while there are some cases where the new reconstructions reduce the approximation error, there are some examples where they actually increase the error. In particular, using a test case from [15], we show that the approximate solution obtained with the weighted power ENO reconstruction, may not converge to the viscosity solution at all.

The structure of this paper is as follows. In Section 2 we review the numerical flux of [14] in one and two dimensions. Section 3 reviews three high-order reconstructions: the WENO method from [6], the mapped WENO method from [11], and the weighted power ENO methods from [26,27]. Numerical simulations, comparing these interpolants, are found in Section 4. We observe that the WENO method works well in all cases, but is improved somewhat by the mapped WENO technique. The weighted power ENO methods work for some examples, but fail for others.

2. The numerical flux

2.1. One-dimensional schemes

We are interested in approximating solutions of the one-dimensional HJ equation

$$\phi_t(x,t) + H(\phi_x) = 0, \quad x \in \mathbb{R}, \tag{2}$$

subject to the initial data $\phi(x, t=0) = \phi_0(x)$. We briefly review the construction of the semi-discrete central scheme of [14] (see also [16]). For simplicity we assume a uniform grid in space and time with mesh spacings, Δx and Δt, respectively. Denote the grid points by $x_i = i\Delta x$, $t^n = n\Delta t$. Let φ_i^n denote the approximate value of $\phi(x_i, t^n)$, and at a fixed time t^n let φ_i' denote the approximate value of the derivative $\phi_x(x_i, t^n)$.

Assume that the approximate solution at time t^n, φ_i^n, is given. The first step is to reconstruct a continuous piecewise-polynomial interpolant $\tilde{\varphi}(x, t^n)$ from the data φ_i^n. We postpone the discussion on the reconstruction of $\tilde{\varphi}(x, t^n)$ to Section 3.

At every grid point x_i we proceed by estimating the maximal local speed of propagation to right, a_i^+, and to the left, a_i^-. For example, for a convex Hamiltonian, these velocities are given by

$$a_i^+ = \max\{H'(\varphi_i'^-), H'(\varphi_i'^+), 0\}, \qquad a_i^- = |\min\{H'(\varphi_i'^-), H'(\varphi_i'^+), 0\}|. \tag{3}$$

Here, $\varphi_i'^{\pm}$ are the one-sided derivatives that can be determined from $\tilde{\varphi}(x, t^n)$. The local speeds of propagation, $a_i^{\pm}$, define two evolution points around each grid point x_i, $x_i^{\pm} = x_i \pm a_i^{\pm}\Delta t$. An exact evolution of $\tilde{\varphi}$ according to (2) at the evolution points $x_i^{\pm}$ reads:

$$\varphi(x_i^{\pm}, t^{n+1}) = \varphi(x_i^{\pm}, t^n) - \int_{t^n}^{t^{n+1}} H(\varphi_x(x_i^{\pm}, t))\,\mathrm{d}t. \tag{4}$$

The first term on the RHS of (4), $\varphi(x_i^{\pm}, t^n)$, is given by the reconstruction. Since the evolution is performed away from the discontinuities (as long as the time step is sufficiently small), the second term on the RHS of (4), i.e., the integral over the Hamiltonian, can be replaced by a quadrature.

The next step is to project $\varphi(x_i^{\pm}, t^{n+1})$ back onto the original grid points, x_i, using a suitable weighted average (or a more complicated procedure as described in [2]). The semi-discrete scheme that is obtained in the limit $\Delta t \to 0$ is

$$\frac{\mathrm{d}}{\mathrm{d}t}\varphi_i(t) = -\left[\frac{a_i^-}{a_i^+ + a_i^-}H(\varphi_i'^+) + \frac{a_i^+}{a_i^+ + a_i^-}H(\varphi_i'^-)\right] + \frac{a_i^+ a_i^-}{a_i^+ + a_i^-}(\varphi_i'^+ - \varphi_i'^-). \tag{5}$$

2.2. Multi-dimensional schemes

The extension of the one-dimensional scheme (5), to an arbitrary number of dimensions in space is straightforward though technical. Here, we summarize the two-dimensional scheme [14]. The details of the general multi-dimensional case can be found in [6].

Here, we are interested in approximating solutions of the two-dimensional HJ equation

$$\phi_t + H(\nabla\phi) = 0, \quad x \in \mathbb{R}^2, \tag{6}$$

subject to the initial data $\phi(x, y, t = 0) = \phi_0(x, y)$. For simplicity we assume a uniform Cartesian grid with mesh spacings Δx and Δy in the x and y directions, respectively. We further assume a given time-step Δt, and let $\varphi_{i,j}^n$ denote the approximate value of $\phi(i\Delta x, j\Delta y, n\Delta t)$.

Similarly to the one-dimensional case, the first step is to reconstruct a two-dimensional interpolant $\tilde{\varphi}(x, y, t^n)$ from the given data $\varphi_{i,j}^n$. We will comment on constructing high-order, multi-dimensional interpolants in Section 3. This interpolant determines the maximum local speed of propagation of information in each direction. We denote by $a_{i,j}^{\pm}$ the local speed of propagation from $x_{i,j}$ in the x-direction (to the left and to the right) and by $b_{i,j}^{\pm}$, the local speed of propagation from $x_{i,j}$ in the y-direction. These quantities also depend on the time t^n, an index which we omit to simplify the notations. For example, with a convex HJ problem, it is possible to estimate the local speeds of propagation as

$$\begin{aligned} a_{i,j}^+ &= \max_{\pm}\{H_x(\varphi_x^{\pm}, \varphi_y^{\pm}), 0\}, \qquad a_{i,j}^- = |\min_{\pm}\{H_x(\varphi_x^{\pm}, \varphi_y^{\pm}), 0\}|, \\ b_{i,j}^+ &= \max_{\pm}\{H_y(\varphi_x^{\pm}, \varphi_y^{\pm}), 0\}, \qquad b_{i,j}^- = |\min_{\pm}\{H_y(\varphi_x^{\pm}, \varphi_y^{\pm}), 0\}|, \end{aligned} \tag{7}$$

where the maximum and minimum are taken over all permutations of $\pm$. The derivatives $\varphi_x^{\pm}$ and $\varphi_y^{\pm}$ are given by the reconstruction $\tilde{\varphi}$. These velocities define four evolution points around each grid point.

We can now repeat the same steps as in the derivation of the one-dimensional scheme. First, the interpolant $\tilde{\varphi}$ is evolved at the evolution points according to (6). The integrals over the fluxes are replaced by quadratures, and the limit as $\Delta t \to 0$ is computed. The resulting semi-discrete scheme (suppressing the indices i, j) is

$$\begin{aligned} \frac{\mathrm{d}\varphi}{\mathrm{d}t} = {} & \frac{a^+a^-}{(a^+ + a^-)}(\varphi_x^+ - \varphi_x^-) + \frac{b^+b^-}{(b^+ + b^-)}(\varphi_y^+ - \varphi_y^-) \\ & - \frac{a^-b^-H(\varphi_x^+, \varphi_y^+) + a^+b^-H(\varphi_x^-, \varphi_y^+)}{(a^+ + a^-)(b^+ + b^-)} + \frac{a^-b^+H(\varphi_x^+, \varphi_y^-) + a^+b^+H(\varphi_x^-, \varphi_y^-)}{(a^+ + a^-)(b^+ + b^-)}. \end{aligned} \tag{8}$$

3. Reconstructions

The derivation of the semi-discrete schemes (5), (8), does not depend on the particular choice of interpolants $\tilde{\varphi}$. The order of accuracy of these schemes is determined by the accuracy of the reconstruction $\tilde{\varphi}$ and the order of accuracy of the ODE solver.

In this section we review the one-dimensional reconstructions that will be combined with the scheme (5): the WENO reconstruction from [6], the weighted power ENO scheme [27] and the mapped ENO reconstruction [11]. We focus on fifth-order methods, which means that we need a fifth-order approximation of the derivative φ' (and a suitable ODE solver). Similar ideas work for other orders of accuracy.

The extension to more than one dimension is straightforward: all computations can be done direction-by-direction. We refer to [6] for more details on the WENO reconstruction. The extension of the weighted power ENO and the mapped WENO reconstructions are also done direction-by-direction.

3.1. The WENO reconstruction

We first consider the WENO reconstruction from [6]. This reconstruction will be used as our base scheme for the other WENO-type reconstructions. The variant we consider here differs from that in [12] only in the definition of the smoothness measures.

Assume three polynomial approximations to the derivative φ'

$$\varphi'^{+}_{k,i} = \frac{1}{\Delta x}\sum_{r=1}^{4} b^{+}_{k,r}\varphi_{i-4+k+r}, \qquad \varphi'^{-}_{k,i} = \frac{1}{\Delta x}\sum_{r=1}^{4} b^{-}_{k,r}\varphi_{i-5+k+r}, \tag{9}$$

$k = 1, 2, 3$, such that they are all third-order accurate, i.e.,

$$\varphi'^{\pm}_{k,i} = \varphi'(x_i) + \mathrm{O}\big(\Delta x^3\big).$$

Here $\varphi'^{+}_{k,i}$ and $\varphi'^{-}_{k,i}$ are approximations to φ' on, respectively, right-biased and left-biased stencils. The coefficients $b^{\pm}_{k,r}$ are given in Table 1. It is then possible to write a linear combination of the polynomials (9) using the "ideal weights" $c^{\pm}_{k}$ (given in Table 2) such that

$$\hat{\varphi}'^{\pm}_{i} := \sum_{k=1}^{3} c^{\pm}_{k}\varphi'^{\pm}_{k,i} = \varphi_x(x_i) + \mathrm{O}\big(\Delta x^5\big). \tag{10}$$

In order to suppress spurious oscillations, the coefficients in (10) are replaced by nonlinear weights, which are set as to preserve the order of accuracy of the reconstruction in smooth regions while automatically switching to stencils that do not cross discontinuities in non-smooth regions. This can be done by defining the convex combination

$$\varphi'^{\pm}_{i} = \sum_{k=1}^{3} w^{\pm}_{k,i}\varphi'^{\pm}_{k,i}, \quad w^{\pm}_{k,i} \geqslant 0, \quad \sum_{k=1}^{3} w^{\pm}_{k,i} = 1. \tag{11}$$

Table 1
Coefficients for the third-order interpolants (9)

	$r=1$	$r=2$	$r=3$	$r=4$		$r=1$	$r=2$	$r=3$	$r=4$
b^{+}_{1}	$\frac{1}{6}$	-1	$\frac{1}{2}$	$\frac{1}{3}$	b^{-}_{1}	$\frac{1}{3}$	$-\frac{3}{2}$	3	$-\frac{11}{6}$
b^{+}_{2}	$-\frac{1}{3}$	$-\frac{1}{2}$	1	$-\frac{1}{6}$	b^{-}_{2}	$-\frac{1}{6}$	1	$-\frac{1}{2}$	$-\frac{1}{3}$
b^{+}_{3}	$-\frac{11}{6}$	3	$-\frac{3}{2}$	$\frac{1}{3}$	b^{-}_{3}	$\frac{1}{3}$	$\frac{1}{2}$	-1	$\frac{1}{6}$

Table 2
The ideal weights for the interpolant (10)

	$k=1$	$k=2$	$k=3$		$k=1$	$k=2$	$k=3$
c^{+}	0.3	0.6	0.1	c^{-}	0.1	0.6	0.3

When the stencil supporting $\varphi'^{\pm}_{k,i}$ contains a singularity, the weight of the more oscillatory polynomial should vanish. Following [13,23], these requirements are met by setting

$$w^{\pm}_{k,i} = \frac{\alpha^{\pm}_{k,i}}{\sum_l \alpha^{\pm}_{l,i}}, \quad \alpha^{\pm}_{k,i} = \frac{c^{\pm}_k}{(\varepsilon + S^{\pm}_{k,i})^p}, \tag{12}$$

where $k, l \in \{1, 2, 3\}$. It is common to choose ε as 10^{-6} in order to prevent the denominator in (12) from vanishing, and set $p = 2$ (see [13]). The smoothness measures $S^{\pm}_{k,i}$ should be large when φ is nearly singular. Following [13], we take $S^{\pm}_{k,i}$ to be the sum of the squares of the L^2-norms of the derivatives on the stencil supporting $\varphi'^{\pm}_{k,i}$. Using the following notations for the forward and backward differences $\Delta^+\varphi_i := \varphi_{i+1} - \varphi_i$ and $\Delta^-\varphi_i := \varphi_i - \varphi_{i-1}$, we approximate the first derivative at x_i by $\Delta^+\varphi_i/\Delta x$ and the second derivative by $\Delta^+\Delta^-\varphi_i/(\Delta x)^2$. We then define the smoothness measure

$$S_i[r, s] = \Delta x \sum_{j=r}^{s} \left(\frac{1}{\Delta x} \Delta^+ \varphi_{i+j} \right)^2 + \Delta x \sum_{j=r+1}^{s} \left(\frac{1}{\Delta x^2} \Delta^+ \Delta^- \varphi_{i+j} \right)^2. \tag{13}$$

Using the notation in (13), for the right-biased interpolant we have $S^+_{1,i} = S_i[-2, 0]$, $S^+_{2,i} = S_i[-1, 1]$ and $S^+_{3,i} = S_i[0, 2]$, while for the left-biased interpolant we have $S^-_{1,i} = S_i[-3, -1]$, $S^-_{2,i} = S_i[-2, 0]$ and $S^-_{3,i} = S_i[-1, 1]$.

3.2. Mapped WENO

A method of improving the accuracy of the WENO reconstruction was recently presented for conservation laws in [11]. This method modifies the WENO weights $w^{\pm}_{k,i}$ via the function

$$g_c(w) := \frac{w(c + c^2 - 3cw + w^2)}{c^2 + w(1 - 2c)}. \tag{14}$$

This function has the properties

$$g_c(0) = 0, \qquad g_c(1) = 1, \qquad g_c(c) = c, \qquad g'_c(c) = g''_c(c) = 0.$$

Given ideal weights $c^{\pm}_k$ and WENO weights $w^{\pm}_{k,i}$ from a base scheme such (9), (11) and (12), we define the mapped WENO weights $\tilde{w}^{\pm}_{k,i}$

$$\tilde{w}^{\pm}_{k,i} = \frac{\tilde{\alpha}^{\pm}_{k,i}}{\sum_{k=1}^{3} \tilde{\alpha}^{\pm}_{k,i}}, \quad \tilde{\alpha}^{\pm}_{k,i} := g_{c^{\pm}_k}(w^{\pm}_{k,i}). \tag{15}$$

Assuming that $w^{\pm}_{k,i} = c^{\pm}_k + \mathrm{O}(\Delta x)$, a Taylor expansion around $c^{\pm}_k$ shows that

$$g_{c^{\pm}_k}\big(w^{\pm}_{k,i}\big) = c^{\pm}_k + \mathrm{O}\big(\Delta x^3\big),$$

which implies that $\tilde{w}^{\pm}_{k,i} = c^{\pm}_k + \mathrm{O}(\Delta x^3)$. This increase in the accuracy with which $\tilde{w}^{\pm}_{k,i}$ approximates the ideal weights $c^{\pm}_k$ leads to an increase in the overall accuracy of the scheme. The fifth-order mapped WENO reconstruction is given by

$$\varphi'^{\pm}_i = \sum_{k=1}^{3} \tilde{w}^{\pm}_{k,i} \varphi'^{\pm}_{k,i}. \tag{16}$$

3.3. Weighted power ENO

Another method of improving the accuracy of WENO reconstructions is the weighted power ENO reconstruction developed for conservation laws in [26] and recently applied to Hamilton–Jacobi equations (with upwind fluxes) in [27]. The basic idea of the power ENO scheme is to apply an extended class of limiters to classical ENO schemes

in order to improve the algorithmic behavior near discontinuities. weighted power ENO methods are based on the limiter

$$\text{powermod}_p(x, y) := \frac{\text{sign}(x) + \text{sign}(y)}{2}\,\text{power}_p\big(|x|, |y|\big), \tag{17}$$

where

$$\text{power}_p(x, y) = \frac{x+y}{2}\left(1 - \left|\frac{x-y}{x+y}\right|^p\right), \quad x, y \geqslant 0.$$

It is easy to see that $\text{powermod}_1(x, y) = \text{minmod}(x, y)$, which is the standard minmod limiter defined as

$$\text{minmod}(x_1, \ldots, x_n) = \begin{cases} \min_i x_i, & x_i > 0, \forall i, \\ \max_i x_i, & x_i < 0, \forall i, \\ 0, & \text{otherwise.} \end{cases}$$

We also have

$$\text{powermod}_\infty(x, y) := \lim_{p\to\infty} \text{powermod}_p(x, y) = \frac{x+y}{2}, \tag{18}$$

see [26] for more details. In [27], the powermod limiter is used to construct a WENO method as follows. We introduce the following notation for the differences:

$$\begin{aligned} &z_{i+1/2} := \frac{\varphi_{i+1} - \varphi_i}{\Delta x}, \qquad d_i := z_{i+1/2} - z_{i-1/2}, \qquad d_{i+1/2} := \frac{d_i + d_{i+1}}{2}, \\ &D_{i+1/2} := d_{i+1} - d_i, \qquad P_j := \text{powermod}_p(D_{i-1/2}, D_{i+1/2}). \end{aligned} \tag{19}$$

Then third-order stencils are constructed as

$$\begin{aligned} \varphi'^{+}_{1,i} &= z_{i+1/2} - \frac{1}{2}d_i - \frac{1}{6}P_i, & \varphi'^{-}_{3,i} &= z_{i-1/2} + \frac{1}{2}d_{i-1} + \frac{1}{3}P_{i-1}, \\ \varphi'^{+}_{2,i} &= z_{i+1/2} - \frac{1}{2}d_{i+1/2} + \frac{1}{12}D_{i+1/2}, & \varphi'^{-}_{2,i} &= z_{i-1/2} + \frac{1}{2}d_{i-1/2} + \frac{1}{12}D_{i-1/2}, \\ \varphi'^{+}_{3,i} &= z_{i+1/2} - \frac{1}{2}d_{i+1} + \frac{1}{3}P_{i+1}, & \varphi'^{-}_{1,i} &= z_{i-1/2} + \frac{1}{2}d_i - \frac{1}{6}P_i. \end{aligned} \tag{20}$$

For this interpolant the ideal weights are $c_1^+ = 0.6$, $c_2^+ = c_3^+ = 0.2$ and $c_1^- = c_2^- = 0.2$, $c_3^- = 0.6$. The nonlinear weights for this method are given by (12) with the smoothness measures

$$\begin{aligned} S^+_{1,i} &= \frac{13}{12}P_i^2 + \frac{1}{4}(2z_{i+1/2} - 2z_{i-1/2} + P_i)^2, \\ S^+_{2,i} &= \frac{13}{12}(z_{i-1/2} - 2z_{i+1/2} + z_{i+3/2})^2 + \frac{1}{4}(z_{i-1/2} - z_{i+1/2})^2, \\ S^+_{3,i} &= \frac{13}{12}P_{i+1}^2 + \frac{1}{4}(2z_{i+3/2} - 2z_{i+1/2} + P_{i+1})^2, \end{aligned} \tag{21}$$

and $S^-_{k,i} = S^+_{1,i-1}$.

The resulting method, denoted Wpower$_p$ENO, is fifth-order accurate for $p \geqslant 3$, see [27]. Following [27] we shall examine this method for $p = 3$ and $p = \infty$ in Section 4. In [26], numerical experiments show that the Wpower$_3$ENO maintains high-order at singularities, in contrast to the original WENO method of [13]. The result is greater accuracy near singularities. However, [26] also points out that the use of limiters in the reconstruction does result in a noisier convergence.

4. Numerical simulations

In this section we compare the various reconstructions from Section 3 for one and two-dimensional Hamilton–Jacobi equations. In all cases we use the central semi-discrete flux from Section 2, integrated in time with a fourth-order strong stability preserving Runge–Kutta method [9]. For the convergence studies we use a time step $\Delta t \propto \Delta x^{5/4}$ in order to show the fifth-order spatial convergence. We concentrate on behavior before singularity formation in nonlinear problems. There is little difference between the methods we examined after singularity formation, with all the methods behaving similar to the method studied in [6].

4.1. One-dimensional convergence studies

We first perform convergence studies of the various methods for one-dimensional examples. The order of accuracy of these methods is determined from the relative L^1 norm. We investigate the following problems:

(1) *Linear advection.* We consider the one-dimensional linear advection equation,

$$\phi_t + \phi_x = 0, \tag{22}$$

subject to periodic boundary conditions on $[-1, 1]$. We test two initial conditions

$$\phi(x, t = 0) = \sin(\pi x), \tag{23}$$

and

$$\phi(x, t = 0) = \sin\left(\pi x - \frac{\sin(\pi x)}{\pi}\right). \tag{24}$$

The latter initial condition, (24), is designed so that the first and third derivatives do not vanish at the same point [11]. As shown in [11] this property reduces the order of accuracy of the smoothness indicators, and consequently it reduces the order of accuracy of the standard WENO method.

(2) *A convex Hamiltonian.* Here, we consider the one-dimensional equation

$$\phi_t + \frac{1}{2}(\phi_x + 1)^2 = 0, \tag{25}$$

subject to the initial data $\phi(x, t = 0) = -\cos(\pi x)$ with periodic boundary conditions on $[0, 2]$. The change of variables, $u(x, t) = \phi_x(x, t) + 1$, transforms the equation into the Burgers' equation, $u_t + \frac{1}{2}(u^2)_x = 0$, which can be easily solved via the method of characteristics [25]. The solution develops a singularity in the form of a discontinuous derivative at time $t = \pi^{-2}$.

(3) *A non-convex Hamiltonian.* We consider a non-convex Hamilton–Jacobi equations,

$$\phi_t - \cos(\phi_x + 1) = 0, \tag{26}$$

subject to the initial data $\phi(x, t = 0) = -\cos(\pi x)$ with periodic boundary conditions on $[0, 2]$. Eq. (26) has a smooth solution for $t \lesssim 1.049/\pi^2$, after which a singularity forms. A second singularity forms at $t \approx 1.29/\pi^2$.

Table 3 shows the convergence results for the three examples, when approximated using the WENO method (11), mapped WENO method (16), and the WENO method (11) using the ideal weights in place of the WENO weights.

Table 3
Relative L^1-errors for the WENO method (11), mapped WENO method (16), and the WENO method (11) using the ideal weights in place of the WENO weights

N	WENO		Mapped WENO		Ideal weights	
	L^1-error	order	L^1-error	order	L^1-error	order
	Linear advection with initial data (23), $T = 2$					
100	9.46×10^{-7}	–	1.08×10^{-7}	–	1.10×10^{-7}	–
200	2.92×10^{-8}	5.02	3.32×10^{-9}	5.03	3.34×10^{-9}	5.04
400	9.05×10^{-10}	5.01	1.03×10^{-10}	5.02	1.03×10^{-10}	5.02
	Linear advection with initial data (24), $T = 2$					
100	8.07×10^{-6}	–	1.22×10^{-6}	–	1.32×10^{-6}	–
200	2.62×10^{-7}	4.94	3.94×10^{-8}	4.96	4.01×10^{-8}	5.04
400	8.13×10^{-9}	5.01	1.23×10^{-9}	5.00	1.24×10^{-9}	5.02
	Convex problem (25), $T = 0.8/\pi^2$					
100	3.89×10^{-6}	–	2.07×10^{-6}	–	2.23×10^{-6}	–
200	1.26×10^{-7}	4.95	9.27×10^{-8}	4.48	9.48×10^{-8}	4.56
400	3.93×10^{-9}	5.00	3.33×10^{-9}	4.80	3.33×10^{-9}	4.83

Table 4
Relative L^1-errors for the linear advection problem (22) with initial data (23), (24). $T = 2$

N	Initial data (23)		Initial data (24)	
	L^1-error	order	L^1-error	order
	WENO			
100	9.46×10^{-7}	–	8.07×10^{-6}	–
200	2.92×10^{-8}	5.02	2.62×10^{-7}	4.94
400	9.05×10^{-10}	5.01	8.13×10^{-9}	5.01
800	2.82×10^{-11}	5.01	2.53×10^{-10}	5.01
	Wpower$_3$ENO			
100	2.74×10^{-6}	–	8.16×10^{-4}	–
200	1.60×10^{-7}	4.10	1.74×10^{-3}	−1.09
400	9.44×10^{-9}	4.09	4.54×10^{-4}	1.93
800	5.69×10^{-10}	4.05	1.21×10^{-4}	1.91
	Wpower$_\infty$ENO			
100	4.30×10^{-7}	–	1.07×10^{-3}	–
200	2.14×10^{-8}	4.33	1.73×10^{-3}	−0.69
400	1.08×10^{-9}	4.31	4.88×10^{-4}	1.82
800	7.35×10^{-11}	3.87	1.21×10^{-4}	2.01

Table 5
Relative L^1-errors for the convex problem (25) and for the non-convex problem (26). $T = 0.05$

N	Convex problem (25)		Non-convex problem (26)	
	L^1-error	order	L^1-error	order
	WENO			
40	1.04×10^{-4}	–	7.66×10^{-6}	–
80	3.00×10^{-6}	5.11	2.82×10^{-7}	4.76
160	8.84×10^{-8}	5.09	9.65×10^{-9}	4.87
320	2.74×10^{-9}	5.01	3.16×10^{-10}	4.93
640	8.74×10^{-11}	4.97	1.20×10^{-11}	4.71
	Wpower$_3$ENO			
40	9.07×10^{-5}	–	1.34×10^{-5}	–
80	2.90×10^{-6}	4.97	8.08×10^{-7}	4.05
160	1.01×10^{-7}	4.84	4.29×10^{-8}	4.24
320	3.86×10^{-9}	4.72	1.77×10^{-9}	4.60
640	1.73×10^{-10}	4.48	8.85×10^{-11}	4.32
	Wpower$_\infty$ENO			
40	9.00×10^{-5}	–	1.18×10^{-5}	–
80	2.72×10^{-6}	5.05	5.93×10^{-7}	4.32
160	8.54×10^{-8}	4.99	2.27×10^{-8}	4.71
320	2.86×10^{-9}	4.90	7.94×10^{-10}	4.84
640	9.87×10^{-11}	4.86	3.88×10^{-11}	4.36

We see that while all three methods show good fifth-order convergence, the mapped WENO method has significantly smaller errors. The mapped WENO errors are close to the errors of the ideal weights, confirming that the mapped WENO weights give a good approximation to the ideal weights.

Tables 4 and 5 show convergence results for the WENO, Wpower$_3$ENO and Wpower$_\infty$ENO methods for the four examples. The number of grid points was chosen to allow a direct comparison with the results in [27]. We see that while the Wpower$_p$ENO methods do not show fifth-order convergence for the linear advection problems, they do show near-fifth-order for the non-linear problems. It is interesting to note that the performance of the Wpower$_3$ENO for the

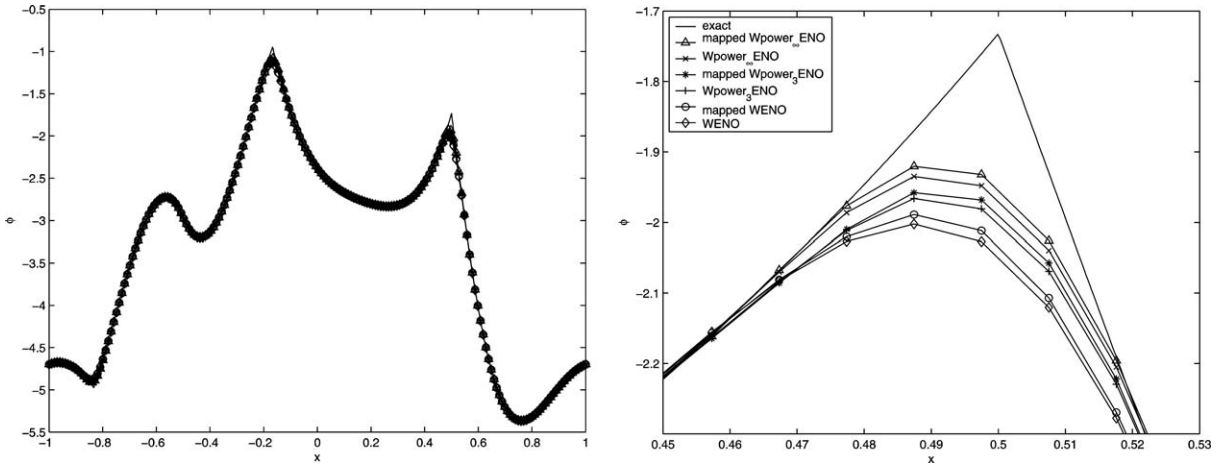

Fig. 1. Linear advection of the initial conditions (27) at $T = 1$ with 200 points. *Left*: The approximation. *Right*: A close-up on the right-most singularity.

advection problem with initial condition (24) is significantly worse than for the initial condition (23). Comparing with the results in [27], which uses a different flux and a different ODE solver, we see the same order of convergence but smaller errors with our central semi-discrete flux and the SSP ODE solver. Mapping improves the Wpower$_p$ENO methods slightly, but not qualitatively. Our base WENO method performs well for all these examples.

4.2. Singularity advection

In this example from [29] we solve the one-dimensional linear advection equation (22), on $[-1, 1]$, subject to periodic boundary conditions. The initial data is taken as $\phi(x, t = 0) = g(x - 0.5)$, where

$$g(x) = -\left(\frac{\sqrt{3}}{2} + \frac{9}{2} + \frac{2\pi}{3}\right)(x + 1) + h(x),$$

and

$$h(x) = \begin{cases} 2\cos(\frac{3\pi}{2}x^2) - \sqrt{3}, & -1 < x < -\frac{1}{3}, \\ 3/2 + 3\cos(2\pi x), & -\frac{1}{3} < x < 0, \\ 15/2 - 3\cos(2\pi x), & 0 < x < \frac{1}{3}, \\ (28 + 4\pi + \cos(3\pi x))/3 + 6\pi x(x - 1), & \frac{1}{3} < x < 1. \end{cases} \tag{27}$$

The results that we obtained with the different reconstructions at $T = 1$ with 200 points are shown in Fig. 1. Note that in this example we also show results that are obtained by composing the Wpower$_p$ENO methods with the mapped WENO method. Clearly, in this example the Wpower$_p$ENO methods show better resolution at the singularities. Wpower$_3$ENO has better resolution than WENO, while Wpower$_\infty$ENO shows the best resolution. Applying WENO mapping slightly improves the resolution of all the methods.

4.3. Convergence to the viscosity solution

An interesting non-convex example is presented in [15]:

$$H(p) = \begin{cases} \frac{p(1-p)}{4}, & p \leqslant \frac{1}{2}, \\ \frac{p(p-1)}{2} + \frac{3}{16}, & \text{otherwise}, \end{cases} \tag{28}$$

subject to the initial data

$$\phi(x, t = 0) = \begin{cases} x - \frac{1}{4}, & x \leqslant \frac{1}{4}, \\ 0, & \text{otherwise}. \end{cases} \tag{29}$$

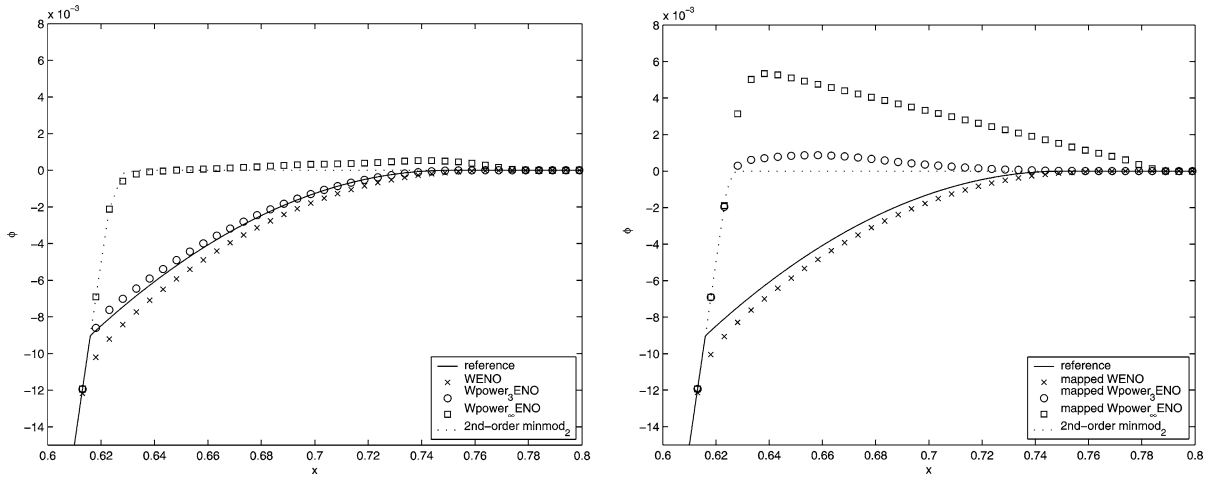

Fig. 2. Approximations to the solution of the problem (28)–(29) at $T = 2$ with 200 points. *Left*: Unmapped reconstructions. *Right*: Mapped reconstructions.

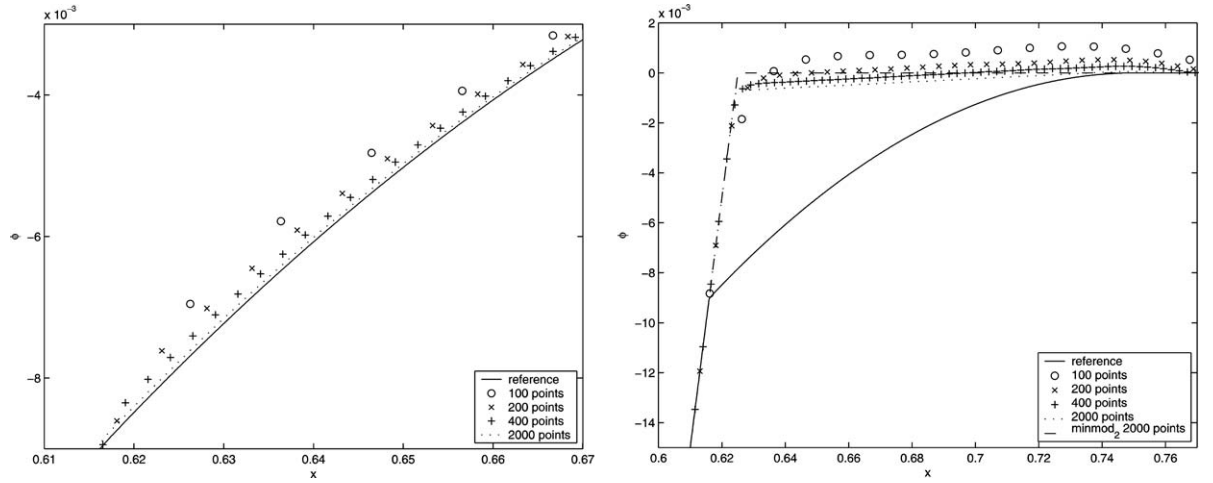

Fig. 3. Convergence of the approximation of the problem (28)–(29) at $T = 2$. *Left*: Wpower$_3$ENO. *Right*: Wpower$_\infty$ENO.

The computational domain is $[0, 1]$ with constant Neumann boundary conditions. The exact viscosity solution is composed (from left to right) of a linear piece, a parabolic piece, and a constant state. In [15] it is shown that the second-order method from [2], using the limiter

$$\text{minmod}_\theta := \text{minmod}(\theta a, b, \theta c), \tag{30}$$

converges to the viscosity solution for $\theta = 1$ but converges to a different solution for $\theta = 2$. We note in passing that we also observe this behavior for several methods using the minmod$_\theta$ limiter, including those found in [3,14,22].

Fig. 2 shows the behavior of the methods discussed in this paper for problem (28)–(29) at $T = 2$ using 200 points. Shown is the parabolic portion of the solution. We compare the WENO methods with a reference solution that is computed with the second-order method from [14] based on minmod$_1$ using 10 000 points. We also show the incorrect solution that is obtained when using the minmod$_2$ limiter. We see that our WENO interpolant and the Wpower$_3$ENO interpolant approximate the correct viscosity solution, while the Wpower$_\infty$ENO is closer to the incorrect solution picked out by minmod$_2$. The effect of WENO mapping is to slightly improve our WENO interpolant. It does cause Wpower$_3$ENO to miss the viscosity solution and to increase the error for the Wpower$_\infty$ENO interpolant.

Fig. 3 shows the convergence of the (unmapped) Wpower$_p$ENO methods for problem (28)–(29) at $T = 2$. This figure indicates that Wpower$_3$ENO converges to the viscosity solution while Wpower$_\infty$ENO does not.

Table 6
Relative L^1-errors for advection of the 2D non-convex problem (31). $T = 0.05$

N	Unmapped		Mapped	
	L^1-error	order	L^1-error	order
	WENO			
40	3.03×10^{-5}	–	2.47×10^{-5}	–
80	1.69×10^{-6}	4.16	1.52×10^{-6}	4.03
160	5.53×10^{-8}	4.93	4.80×10^{-8}	4.98
	$\text{Wpower}_3\text{ENO}$			
40	2.80×10^{-5}	–	2.51×10^{-5}	–
80	1.74×10^{-6}	4.01	1.74×10^{-6}	3.85
160	6.55×10^{-8}	4.73	6.59×10^{-8}	4.72
	$\text{Wpower}_\infty\text{ENO}$			
40	2.49×10^{-5}	–	2.30×10^{-5}	–
80	1.64×10^{-6}	3.92	1.64×10^{-6}	3.81
160	5.38×10^{-8}	4.93	5.35×10^{-8}	4.93

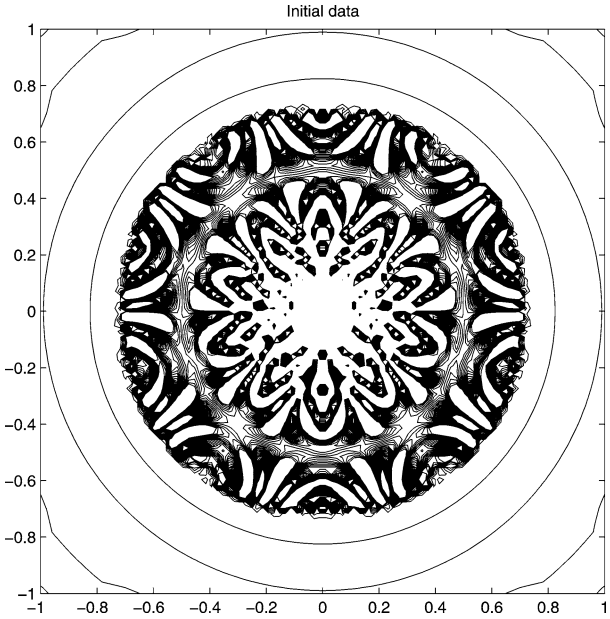

Fig. 4. Contours of the mean curvature of the initial data for problem (32).

4.4. Two-dimensional problems

A non-convex Hamiltonian

We consider a two-dimensional, non-convex problem that is analogous to the one-dimensional problem (26),

$$\phi_t - \cos(\phi_x + \phi_y + 1) = 0. \tag{31}$$

We assume the initial data $\phi(x, y, 0) = -\cos(\pi(x + y)/2)$, and periodic boundary conditions. Results for the various methods are given in Table 6.

The reinitialization problem

We consider the "level set reinitialization" problem [27],

$$\phi_t + \text{sign}(\phi_0)\big[\sqrt{\phi_x^2 + \phi_y^2} - 1\big] = 0. \tag{32}$$

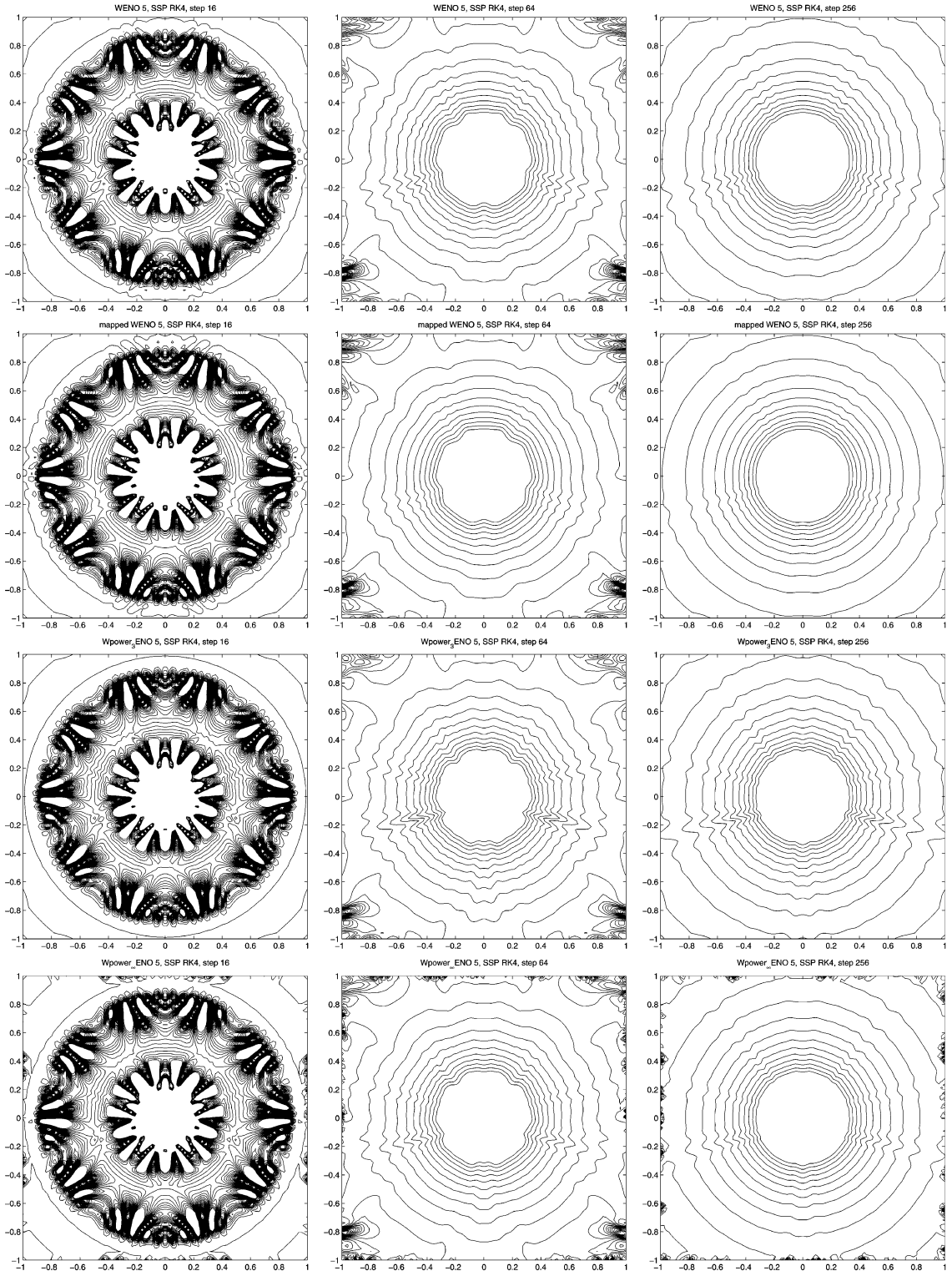

Fig. 5. Contours of mean curvature of the reinitialization problem (32). *Top to bottom*: WENO, Mapped WENO, Wpower$_3$ENO, Wpower$_\infty$ENO. *Left to right*: 16, 64 and 256 time steps.

Subject to the initial data

$$\phi(x, t=0) = \phi_0 := \begin{cases} d+\delta, & |d| < \varepsilon, \\ d, & \text{otherwise.} \end{cases} \tag{33}$$

Here, $d = \sqrt{x^2+y^2} - 0.5$, $\delta = \frac{\varepsilon}{16\pi}\sin(\frac{4\pi d \sin 5\theta}{\varepsilon})$, $\theta = \tan^{-1}(y/|x|)$ and $\varepsilon = 0.2$. This problem arises in level set methods, where it is highly desirable that initial noise in the mean curvature of ϕ be damped during the evolution of (32). The initial data is chosen to introduce noise in order to study this damping.

In Figs. 4 and 5 we show contours of the regularized mean curvature

$$\kappa := \nabla \cdot \frac{\nabla\phi}{\sqrt{|\nabla\phi|^2 + \Delta x^2}}.$$

Fig. 4 shows the noisy initial data, while 5 shows the evolution after a fixed numbers of time steps. We see that the mapped WENO reconstruction gives us the least noisy results after 256 time steps.

References

[1] R. Abgrall, Numerical discretization of the first-order Hamilton–Jacobi equation on triangular meshes, Comm. Pure Appl. Math. 49 (1996) 1339–1373.

[2] S. Bryson, A. Kurganov, D. Levy, G. Petrova, Semi-discrete central-upwind schemes with reduced dissipation for Hamilton–Jacobi equations, IMA Journal of Numerical Analysis 25 (2005) 113–138.

[3] S. Bryson, D. Levy, Central schemes for multi-dimensional Hamilton–Jacobi equations, SIAM J. Sci. Comput. 25 (2003) 767–791.

[4] S. Bryson, D. Levy, High-order central WENO schemes for 1D Hamilton–Jacobi equations, in: F. Brezzi, et al. (Eds.), Numerical Mathematics and Advanced Applications, Proceedings of ENUMATH 2001, Ischia, Italy, Springer, Italy, 2003, pp. 45–54.

[5] S. Bryson, D. Levy, High-order central WENO schemes for multi-dimensional Hamilton–Jacobi equations, SIAM J. Numer. Anal. 41 (2003) 1339–1369.

[6] S. Bryson, D. Levy, High-order semi-discrete central-upwind schemes for multi-dimensional Hamilton–Jacobi equations, J. Comput. Phys. 189 (2003) 63–87.

[7] M.G. Crandall, H. Ishii, P.-L. Lions, User's guide to viscosity solutions of second order partial differential equations, Bull. Amer. Math. Soc. 27 (1992) 1–67.

[8] M.G. Crandall, P.-L. Lions, Viscosity solutions of Hamilton–Jacobi equations, Trans. Amer. Math. Soc. 277 (1983) 1–42.

[9] S. Gottlieb, C.-W. Shu, E. Tadmor, Strong stability-preserving high order time discretization methods, SIAM Review 43 (2001) 89–112.

[10] A. Harten, B. Engquist, S. Osher, S. Chakravarthy, Uniformly high order accurate essentially non-oscillatory schemes III, J. Comput. Phys. 71 (1987) 231–303.

[11] A.K. Henrick, T.D. Aslam, J.M. Powers, Mapped weighted essentially non-oscillatory schemes: Achieving optimal order near critical points, J. Comput. Phys. 207 (2005) 542–567.

[12] G.-S. Jiang, D. Peng, Weighted ENO schemes for Hamilton–Jacobi equations, SIAM J. Sci. Comput. 21 (2000) 2126–2143.

[13] G.-S. Jiang, C.-W. Shu, Efficient implementation of weighted ENO schemes, J. Comput. Phys. 126 (1996) 202–228.

[14] A. Kurganov, S. Noelle, G. Petrova, Semi-discrete central-upwind schemes for hyperbolic conservation laws and Hamilton–Jacobi equations, SIAM J. Sci. Comput. 23 (2001) 707–740.

[15] A. Kurganov, G. Petrova, Adaptive central-upwind schemes for Hamilton–Jacobi equations with nonconvex Hamiltonians, http://www.math.tulane.edu/~kurganov/pub.html.

[16] A. Kurganov, E. Tadmor, New high-resolution semi-discrete central schemes for Hamilton–Jacobi equations, J. Comput. Phys. 160 (2000) 720–742.

[17] D. Levy, S. Nayak, Central Schemes for Hamilton–Jacobi Equations on Unstructured Grids, in: M. Feistauer, et al. (Eds.), Numerical Mathematics and Advanced Applications, Proceedings of ENUMATH 2003, Prague, Czech Republic, Springer, Berlin, 2004, pp. 623–630.

[18] D. Levy, S. Nayak, C.-W. Shu, Y.-T. Zhang, Central WENO schemes for Hamilton–Jacobi equations on triangular meshes, in preparation.

[19] P.L. Lions, Generalized Solutions of Hamilton–Jacobi Equations, Pitman, London, 1982.

[20] P.L. Lions, P.E. Souganidis, Convergence of MUSCL and filtered schemes for scalar conservation laws and Hamilton–Jacobi equations, Numer. Math. 69 (1995) 441–470.

[21] C.-T. Lin, E. Tadmor, L^1-stability and error estimates for approximate Hamilton–Jacobi solutions, Numer. Math. 87 (2001) 701–735.

[22] C.-T. Lin, E. Tadmor, High-resolution non-oscillatory central schemes for approximate Hamilton–Jacobi equations, SIAM J. Sci. Comput. 21 (2000) 2163–2186.

[23] X.-D. Liu, S. Osher, T. Chan, Weighted essentially non-oscillatory schemes, J. Comput. Phys. 115 (1994) 200–212.

[24] S. Osher, J. Sethian, Fronts propagating with curvature dependent speed: algorithms based on Hamilton–Jacobi formulations, J. Comput. Phys. 79 (1988) 12–49.

[25] S. Osher, C.-W. Shu, High-order essentially nonoscillatory schemes for Hamilton–Jacobi equations, SIAM J. Numer. Anal. 28 (1991) 907–922.

[26] S. Serna, A. Marquina, Power-ENO methods: A fifth-order accurate weighted power ENO method, J. Comput. Phys. 194 (2004) 632–658.

[27] S. Serna, J. Qian, Fifth order weighted power-ENO methods for Hamilton–Jacobi equations, UCLA CAM-Report 04-62, 2004, J. Sci. Comput., submitted for publication.
[28] P.E. Souganidis, Approximation schemes for viscosity solutions of Hamilton–Jacobi equations, J. Diff. Equations 59 (1985) 1–43.
[29] Y.-T. Zhang, C.-W. Shu, High-order WENO schemes for Hamilton–Jacobi equations on triangular meshes, SIAM J. Sci. Comput. 24 (2003) 1005–1030.